Tetrahedron 66 (2010) 6238–6250

Contents lists available at ScienceDirect

Tetrahedron

journal homepage: www.elsevier.com/locate/tet

Detecting solid-state reactivity in 10-hydroxy-10,9-boroxophenanthrene using NMR spectroscopy

Diego Carnevale, Vicente del Amo, Douglas Philp *, Sharon E. Ashbrook *

School of Chemistry and EaStCHEM, University of St Andrews, North Haugh, St Andrews, Fife KY16 9ST, United Kingdom

ARTICLE INFO

Article history:
Received 15 February 2010
Accepted 17 May 2010
Available online 25 May 2010

Keywords:
Self-assembly
Molecular recognition
Aromatic compounds
Solid-state NMR spectroscopy
Reversible reactions
DFT calculations

ABSTRACT

Solid-state NMR spectroscopy and computational methods are used to probe the transformation of 10-hydroxy-10,9-boroxophenanthrene to its corresponding anhydride in the solid state. DFT calculations are used to assist the assignment of the NMR spectra of both these boron-containing heteroaromatic compounds, in solution and in the solid state. Solid-state NMR spectroscopy reveals that the dehydration of crystalline 10-hydroxy-10,9-boroxophenanthrene proceeds at relatively low temperatures—a transformation, that is, undetectable by X-ray diffraction and gravimetric analysis. Computational methods are used to elucidate a plausible reaction pathway for this transformation and to explain its detection only by NMR methods.

1. Introduction

In recent years, supramolecular chemists have attempted to achieve the construction of large, regular, crystalline systems, based purely on the specific and predictable location of appropriate recognition motifs. This process of 'crystal engineering'[1] is a potentially powerful method for preparing assemblies of specified structure or function. Key to the implementation of crystal engineering is an understanding of the different intermolecular interactions that make up the supramolecular chemists' toolbox and a catalogue of the different recognition motifs or 'building blocks' that one may consider exploiting. Although many different motifs for crystal engineering have been reported, there still remains a need for new chemical structures, with novel interaction patterns, that will broaden the choice of building blocks available. As well as the desire to create specific crystal structures predictably, there is also a need to incorporate 'functionality'. In many cases, the new crystalline materials, once assembled through non-covalent interactions, do nothing more. It would be useful, particularly in terms of materials chemistry, if one could take the supramolecular construct and transform[2] it into a permanent, i.e., covalently bonded structure. In general, this goal has proved more difficult to achieve, as the types of interactions used to assemble crystals are often inappropriate for bond forming reactions between molecules.

Our own interest in crystal engineering processes, and, indeed, in self-assembly in general, led us to consider the use of a new class of supramolecular building block based on boron-containing aromatic (BcA) compounds—specifically borazaaromatic and boroxoaromatics (Fig. 1a) in which a C=C bond of an aromatic compound

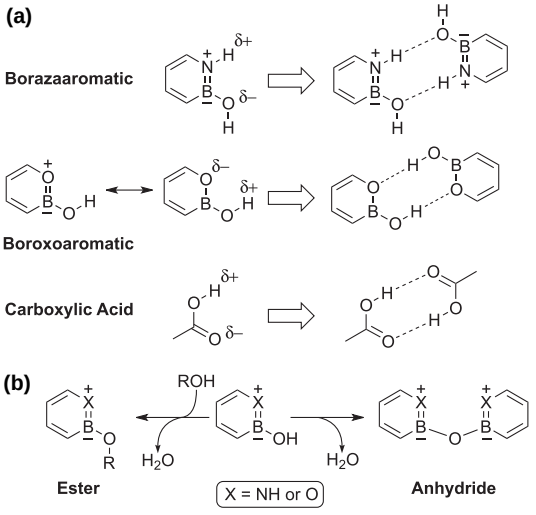

Figure 1. (a) Both boraza- and boroxoaromatic compounds are isosteres of carboxylic acids. (b) Both boraza- and boroxoaromatic compounds exhibit similar chemical reactivity to carboxylic acids, forming esters on reaction with alcohols and the corresponding anhydrides on dehydration.

* Corresponding author. E-mail addresses: d.philp@st-andrews.ac.uk (D. Philp), sema@st-andrews.ac.uk (S.E. Ashbrook).

0040-4020/$ – see front matter © 2010 Elsevier Ltd. All rights reserved.
doi:10.1016/j.tet.2010.05.065

is replaced by either the isoelectronic $^{+}N{=}B^{-}$ or $^{+}O{=}B^{-}$ unit, respectively. These compounds were first synthesized during the 1960s, primarily for their novelty as unusual heteroaromatic compounds, and research into their synthesis and properties had all but ceased by the 1970s. However, we identified two interesting chemical and physical properties that had not been exploited during this original research. In principle, the polarization pattern of the constituent atoms of the hydroxy BcA functionality is remarkably similar to that of carboxylic acids and, hence, we were able to demonstrate[3] that both hydroxyborazaaromatic and hydroxyboroxoaromatic compounds were capable of forming (Fig. 1) cyclic hydrogen-bonded dimers in an manner analogous to the formation of hydrogen-bonded carboxylic acid dimers.

Secondly, we realized that the boron atom of BcAs is evidently quite reactive towards nucleophiles. Extending the analogy with carboxylic acids, BcAs react with themselves to form anhydrides and esters. The literature contains numerous reports of hydroxy BcA compounds in self-condensation reactions to form the corresponding anhydrides (Fig. 1b). Recrystallization of the hydroxy compounds from alcohols, such as methanol and ethanol, is also reported to give the corresponding esters (Fig. 1b). Although the hydroxy BcA functionality is structurally analogous to carboxylic acids, their reactivity would appear to be markedly different; for example, the esterification and the self-condensation of carboxylic acids to form anhydrides in the solid-state, are not normally facile reactions. The latent reactivity exhibited by hydroxy BcAs is, however, a superb means of achieving permanent linkages between the building blocks, i.e., of adding value to the crystal engineering that assembles the building blocks initially.

We were able to demonstrate[4] that 10-hydroxy-10,9-boroxophenanthrene **HBOP** (Fig. 2a) reacts with itself to form the corresponding anhydride **BBE** on heating only in the solid state. The solid-state dehydration reaction involving **HBOP** to form the homoanhydride occurs at temperatures above 60 °C and the rate of reaction is appreciable at temperatures well below the melting point of the compound (around 140 °C). In previous work, we were able to follow this solid-state transformation using thermogravimetric analysis (TGA) (Fig. 2b) and powder X-ray diffraction (PXRD) (Fig. 2c). Although fitting of the kinetic data obtained using these two analytical techniques to the Avrami–Erofe'ev equation[5] afforded a plausible and consistent activation barrier (140 kJ mol^{-1}) for the chemical change occurring within the sample, there were significant inconsistencies associated with the results from the two different techniques, particularly in respect of the rate at which the transformation occurred.

Using the two different techniques, TGA and PXRD, to monitor the solid-state transformation from **HBOP** to **BBE** as a function of time probes different aspects of the system (and monitors the change in a different component of the system as a function of time). Moreover, neither of these techniques actually probes the chemical reaction from **HBOP** to **BBE** directly. Specifically, the isothermal TGA experiment monitors the loss of mass of the sample as a function of time—in this case, the escape of H_2O from the solid sample into the vapour phase. It is important to realize that this loss of H_2O is not necessarily equal to the rate of production of H_2O within the crystals of the reactant **HBOP**. Therefore, the rate of mass loss does not necessarily reflect the rate of the chemical transformation from **HBOP** to **BBE** within the crystal. On the other hand, the PXRD experiment monitors the changing identity of crystalline phases present during the solid-state transformation, and in order to observe sharp lines in the PXRD pattern, it is necessary that crystalline particles of sufficient size are present. Again, the growth of crystalline particles of the product phase **BBE** of sufficient size to give a PXRD pattern characteristic of this phase need not necessarily proceed at the same rate as the actual chemical transformation from **HBOP** to **BBE** within the parent crystal structure. In particular, at sufficiently low values of the extent of reaction, molecules of **BBE** produced by the chemical reaction may be accommodated within

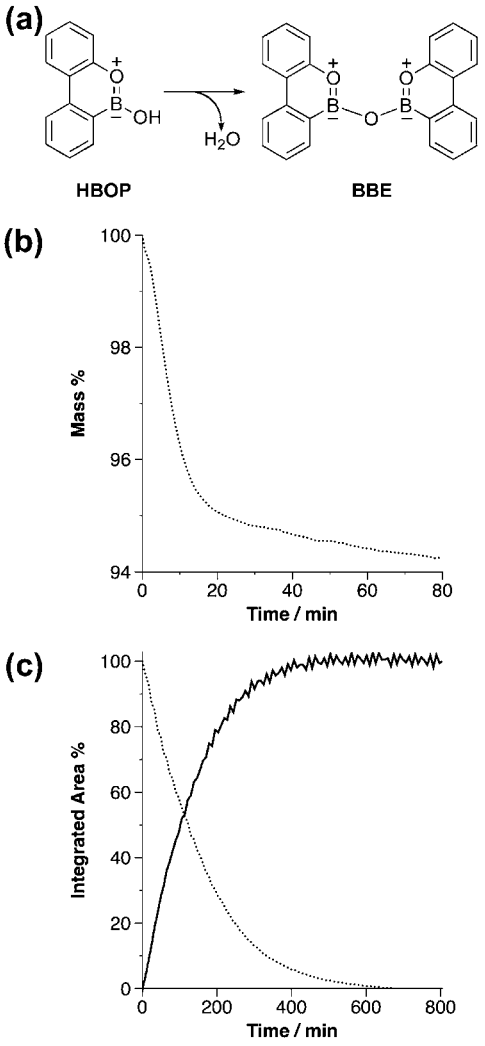

Figure 2. The conversion (a) of 10-hydroxy-10,9-boroxophenanthrene **HBOP** into the corresponding anhydride **BBE** can be monitored either by (b) thermogravimetric analysis or by (c) powder X-ray diffraction. In the case of (c), the transformation can be monitored either by loss of crystalline **HBOP** (dashed line) or by the appearance of crystalline **BBE** (solid line).

the reactant crystal structure of **HBOP** (representing a solid solution of **HBOP** and **BBE**, and, possibly, also containing H_2O molecules produced from the reaction). At this stage, no amount of the crystalline product phase will actually be present, even though molecules of **BBE** have been produced by the chemical reaction, and PXRD will show no evidence for the presence of the product phase. Thus, although both TGA and PXRD can give us some insight into the reaction processes occurring in the solid state, they are not particularly sensitive to the principal chemical transformation itself.

In solution, NMR spectroscopy is an ideal probe of chemical reactivity and, previously, we have utilized[6] this technique to derive important information concerning both reaction mechanism and kinetics. Providing the rate of the chemical reaction under investigation is appropriate, both quantitative and structural information[7] about the reagents, intermediates and products present in solution can be derived directly from the same experiment. Given the ambiguous nature of reporting of the chemical transformation by both TGA and PXRD in the solid-state transformation of **BBE** into **HBOP**, we have become interested in probing this reaction in the solid state by a more direct method. In this respect, solid-state NMR spectroscopy should prove to be a useful tool. However, in contrast to the solution state, where narrow spectral resonances are observed

as a result of the isotropic tumbling motion of molecules, the orientation-dependent (anisotropic) interactions, which affect nuclear spins are retained in the solid state, resulting in broad and often uninformative lineshapes. A number of solutions are commonly employed to alleviate the resulting resolution and sensitivity challenges, including magic angle spinning (MAS),[8] where the sample is physically rotated at an angle of θ=54.736° (the 'magic angle') to the external magnetic field, and decoupling (the manipulation of nuclear spins through R_f irradiation during the acquisition of the NMR signal). However, for quadrupolar nuclei, i.e., those with spin quantum number $I>1/2$, e.g., ^{11}B (I=3/2), MAS is unable to remove completely the quadrupolar interaction (resulting from the interaction of the nuclear electric quadrupole moment with the electric field gradient at the nucleus) and anisotropically-broadened powder-pattern lineshapes remain. In order to achieve high-resolution spectra in these cases more complex two-dimensional techniques, such as the commonly used multiple-quantum MAS (MQMAS)[9] experiment, are required. Despite the resolution and sensitivity challenges associated with NMR in the solid state, the information available on local structure and dynamics can be invaluable to understanding the properties of a solid.

Here, we report our attempts to probe the nature of the chemical transformation that occurs as crystalline **HBOP** is converted to **BBE** more directly using a combination of solid-state NMR spectroscopy and electronic structure calculations.

2. Results and discussion

In order to begin probing the chemical transformation of **HBOP** into **BBE** by NMR spectroscopy, it is necessary to assign fully all of the resonances in the ^{1}H and ^{13}C NMR spectra of these compounds in solution. This assignment will assist in the interpretation of solid-state spectra and also provides a test-bed for assessing the quality of DFT calculations of NMR parameters. For **HBOP**, this assignment could be accomplished readily using a series of standard 1D and 2D experiments (see Supplementary data). The assignment of the resonances observed in the ^{1}H and ^{13}C NMR spectra of **HBOP**, recorded in $CDCl_3$ at room temperature, are given in Table 1, together with the numbering system used to identify the individual sites.

Table 1
Assignment of the resonances observed in the ^{1}H and ^{13}C NMR spectra of **HBOP** recorded in CDCl3 at room temperature and the chemical shifts calculated using the CSGT method at the B3LYP 6-311++G(2d,p) level of theory

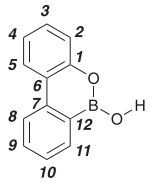

Assignment	Calculated		Experimental	
	^{13}C (ppm)	^{1}H (ppm)	^{13}C (ppm)	^{1}H (ppm)
1	154.0	—	151.2	—
2	119.1	7.32	119.6	7.20
3	128.6	7.33	129.0	7.31
4	121.9	7.14	122.7	7.16
5	123.2	8.17	123.6	8.06
6	124.1	—	123.0	—
7	142.0	—	140.4	—
8	120.7	8.20	121.2	8.10
9	132.3	7.66	132.6	7.64
10	126.5	7.43	127.2	7.40
11	135.2	8.31	133.4	8.01
12	123.4	—	—[a]	—

[a] The resonance arising from C12 cannot being detected in the 1D ^{13}C spectrum as a result of the fast T2 relaxation of the bonded quadrupolar ^{11}B/^{10}B (I=3/2 and I=3, respectively).

With this assignment in hand, we are in a position to assess the reliability of DFT methods in describing these boroxoaromatic systems. Initially, the ^{13}C NMR parameters for **HBOP** itself and the corresponding hydrogen-bonded dimer, (**HBOP**)$_2$, were calculated using the CSGT method,[10] as implemented in the Gaussian03[11] suite of programs, the B3LYP functional and a variety of basis sets. The potential differences between **HBOP** and (**HBOP**)$_2$ are of particular interest, since, in the solid state, **HBOP** is present in the form of hydrogen-bonded dimers, but in solution, the ^{1}H and ^{13}C spectra are presumably fast exchange averages of the spectra from the monomer and the dimer. Given the low dielectric constant of $CDCl_3$ and the lack of any obvious specific interactions between **HBOP** or (**HBOP**)$_2$, we felt that solvent effects on the NMR parameters could largely be discounted. Previously, we have shown[3] that **HBOP** has a strong preference for locating the O–H bond vector in a *syn* orientation with respect to the endocyclic O–B bond and this conformer was therefore chosen for this study. The structures were first optimized at the HF level and the 6-31G basis set and, then, further optimized at the B3LYP/6-311++G(2d,p) level of theory. The calculation of the magnetic shieldings was subsequently performed using the CSGT method and the same hybrid functional at variable basis set sizes to check for the convergence of the values. The calculated parameters for benzene were used to reference the shieldings. It quickly became clear that a triple zeta basis set and the use of valence shell diffuse functions was necessary in order to obtain a good correlation between the experimental and the calculated ^{13}C chemical shifts, and the data summarized in Figure 3 were calculated at the B3LYP/6-311++G(2d,p) level of theory.

The ^{13}C chemical shifts calculated at this level of theory for both the monomeric **HBOP** (Fig. 3a) and the corresponding hydrogen-bonded dimer (**HBOP**)$_2$ (Fig. 3b) show excellent correlations with the experimental solution phase data. It is interesting to note that, although in (**HBOP**)$_2$, two molecules mutually perturb themselves by virtue of the cyclic hydrogen bond network, there is no significant change in the quality of the correlation obtained. Analyzing the differences between the experimental and calculated data more closely, the most significant deviations between experiment and theory are C1, C6, C7 and C11. Whilst one might attribute the deviations associated with C1, C6 and C7 to an imperfect description of the electronic structure of the boroxoaromatic ring, the reasons behind the relatively large deviation associated with C11 is unclear, especially since the shielding of C12, the carbon adjacent to the boron centre, is relatively well described. All carbons show relatively small chemical shift changes (generally $\leq$0.8 ppm) when comparing monomeric **HBOP** and the corresponding hydrogen-bonded dimer (**HBOP**)$_2$. In general, the carbon atoms in (**HBOP**)$_2$ are calculated to be more deshielded than in monomeric **HBOP**. This result is consistent with the planar structure of the hydrogen-bonded dimer, which places one molecule of **HBOP** within the deshielding zone of the ring current of its hydrogen-bonded partner. The carbon that exhibits the largest change (1.26 ppm) is, unsurprisingly, C12, as presumably the formation of the hydrogen bond increases the electron supply to the adjacent boron centre.

The resolution in the ^{13}C solid-state MAS NMR spectrum of **HBOP** (Fig. 4a) is significantly poorer than that observed in solution-state NMR. There is considerable overlap of the spectral resonances, despite the use of both MAS and high-power ^{1}H decoupling, as a consequence not only of the greater inherent linewidth typically observed for solids, but also a result of the complexity of the **HBOP** solid-state structure. In the solid state, **HBOP** exists exclusively as a hydrogen-bonded dimer (**HBOP**)$_2$, with two crystallographically-distinct molecules present in the unit cell. Whilst it may initially be tempting to assign the spectrum shown in Figure 4a by straightforward comparison with the solution-state spectrum, considering only the relative ordering of the isotropic chemical shifts, this approach is deprecated both by the

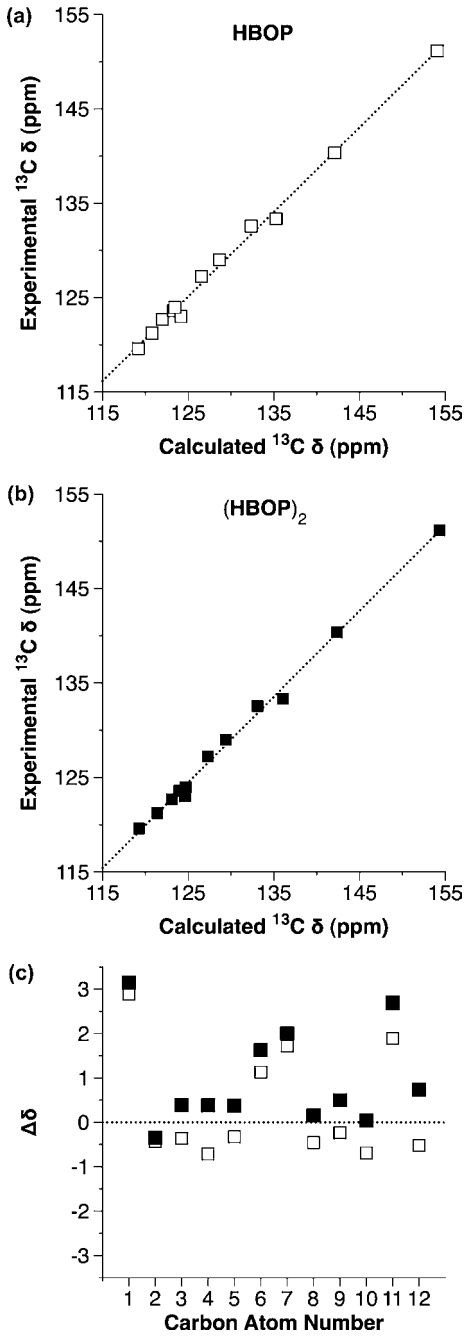

Figure 3. (a) Correlation between the experimental ^{13}C chemical shifts and those calculated for the **HBOP** monomer using the CSGT method at the B3LYP/6-311++G(2d,p) level of theory. (b) Correlation between the experimental ^{13}C chemical shifts and those calculated for the (**HBOP**)$_2$ hydrogen-bonded dimer using the CSGT method at the B3LYP/6-311++G(2d,p) level of theory. (c) Signed differences ($\Delta\delta$) in the ^{13}C chemical shifts for the HBOP monomer (open squares) and the (**HBOP**)$_2$ hydrogen bonded-dimer (filled squares) compared to the chemical shifts observed experimentally for **HBOP** in $CDCl_3$ solution at room temperature.

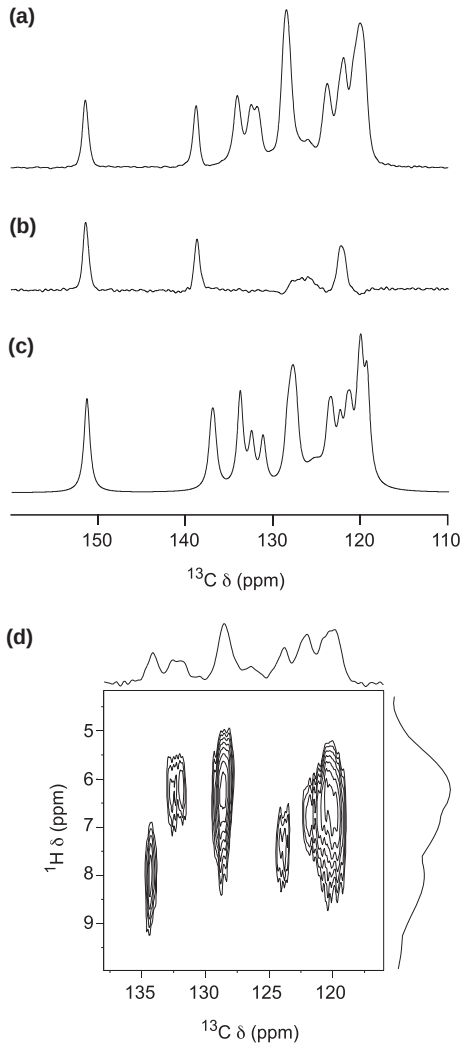

Figure 4. Experimental ^{13}C (9.4 T) (a) MAS and (b) dipolar dephasing MAS NMR spectra of powdered **HBOP**. In each case, spectra were recorded using ramped cross polarization with a contact pulse of 1 ms and with SPINAL64 heteronuclear ^{1}H decoupling. In (b), there was an (undecoupled) interval of 60 μs after the cross-polarization step and prior to the formation of a ^{13}C spin echo (where ^{1}H decoupling was applied), during which the resonances corresponding to ^{13}C species with attached ^{1}H were dephased. The MAS rates were (a) 12 kHz and (b) 6 kHz. (c) ^{13}C (9.4 T) MAS NMR spectrum simulated with the (CASTEP) calculated ^{13}C chemical shifts given in Table 2. For most resonances an inherent linewidth of 80 Hz was assumed (estimated by fitting a resolved resonance in the experimental spectrum), whilst for C12/C12′ (directly bonded to ^{10}B/^{11}B) a larger linewidth of ~280 Hz was employed. (d) Two-dimensional ^{1}H/^{13}C (11.7 T) HETCOR correlation spectrum of solid **HBOP**, with homonuclear ^{1}H FSLG decoupling in the indirect dimension and SPINAL64 heteronuclear ^{1}H decoupling in acquisition. The contact time in the cross polarization step was 100 μs. The MAS rate was 13 kHz.

presence of 24, rather than 12, distinct carbon environments and also by the changes in chemical shift brought about by crystal packing. For example, the ^{13}C resonance at δ=138.8 ppm in the solid-state spectrum is shifted downfield by ~1.5 ppm relative to the corresponding resonance in solution. Although this resonance is clearly resolved in both spectra, similar shift changes in the more crowded regions of the spectrum will then result in incorrect assignments. Insight into the spectral assignment can be obtained by dipolar dephasing experiments where, owing to the reintroduction of the ^{1}H/^{13}C dipolar coupling, only resonances resulting from quaternary carbons are observed (Fig. 4b). Quaternary carbons are observed at δ=151.5, 138.8, 126.1 and 122.5 ppm, with the third of these resulting from C12, which was not observed in solution. Owing to the presence of a large scalar coupling to the directly bonded ^{10}B/^{11}B (I=3 and I=$^{3}/_{2}$, respectively), this resonance is much broader than the others in the spectrum.

In order to gain more detailed insight into the spectral assignment, DFT calculations were once again performed. In contrast to solution, where the shifts calculated for a single isolated molecule can be compared to experiment, in the solid state the full crystal structure must be considered. In order to achieve this goal, calculations were carried out using CASTEP,[12] a planewave pseudopotential code that utilizes periodic boundary conditions to recreate

an infinite crystal structure from a single unit cell. Table 2 shows the calculated isotropic chemical shifts for the 24 distinct carbons (labelled x and x′ to distinguish the two different **HBOP** molecules in the unit cell). The calculations were referenced by setting the

Table 2
Assignment of the resonances observed in the ^{1}H and ^{13}C MAS NMR spectra of powdered **HBOP** and the chemical shifts calculated using GGA PBE within the planewave code CASTEP

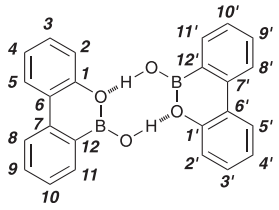

Assignment	Calculated		Experimental[a]	
	^{13}C (ppm)	^{1}H (ppm)	^{13}C (ppm)	^{1}H (ppm)
1	151.4	—	151.5	—
1	151.3			
2	120.1	6.1	120.3	6.4
2′	120.2	6.4		
3	127.5	6.0	128.4[b]	6.2
3′	128.1	6.0		
4	121.3	6.8	121.9	6.7
4′	120.4	6.8	121.4	
5	123.4	7.6	123.8	7.4
5′	123.8	7.6	124.1	
6	122.5	—	122.5	—
6′	121.7			
7	137.2	—	138.8	—
7′	136.9			
8	119.4	7.2	119.6	6.7
8′	119.4	7.0		
9	131.3	6.2	131.8	6.2
9′	132.6	6.3	132.7	
10	128.5	6.5	128.6[b]	6.3
10′	127.8	6.3		
11	133.9	7.8	134.1	8.0
11′	133.9	7.9		
12	125.4	—	126.1	—
12′	125.3			

[a] Estimated errors for the experimental chemical shifts are ± 0.1 ppm (^{13}C) and ±0.2 ppm (^{1}H)
[b] Note there is considerable overlap between these four ^{13}C resonances

average value of the experimental and calculated shifts to be equal, as is common practise when using a periodic approach. Whilst there is a broad similarity between the values calculated for the single molecule and those for the extended solid-state structure, there are some differences, presumably resulting from the presence of the (**HBOP**)$_2$ dimer and the crystal packing. For example, in some cases the ^{13}C chemical shifts calculated for the two **HBOP** molecules within the hydrogen-bonded dimer are different. This difference in chemical shift ($\Delta\delta = \delta(^{13}Cx) - \delta(^{13}Cx')$) is plotted in Figure 5a. While most shift differences are within ±0.5 ppm, a number of carbons do exhibit more significant differences, notably C4, C6, C9 and C10. Many of these carbons are found on the extremities of the dimer molecule and are probably most significantly affected by the π-stacking of the aromatic rings.

Some progress can be made with spectral assignment through a combined consideration of the DFT calculations, the ^{13}C MAS spectrum and associated dipolar dephasing experiments and the $^{1}H/^{13}C$ two-dimensional HETCOR[13] (heteronuclear correlation) spectrum shown in Figure 4d, where magnetization is transferred from ^{1}H to adjacent ^{13}C by cross-polarization. The resolution in the ^{13}C dimension is increased owing to the dispersion of the resonances according to the shift of their associated ^{1}H in the indirect dimension; the spectrum, therefore, contains only non-quaternary

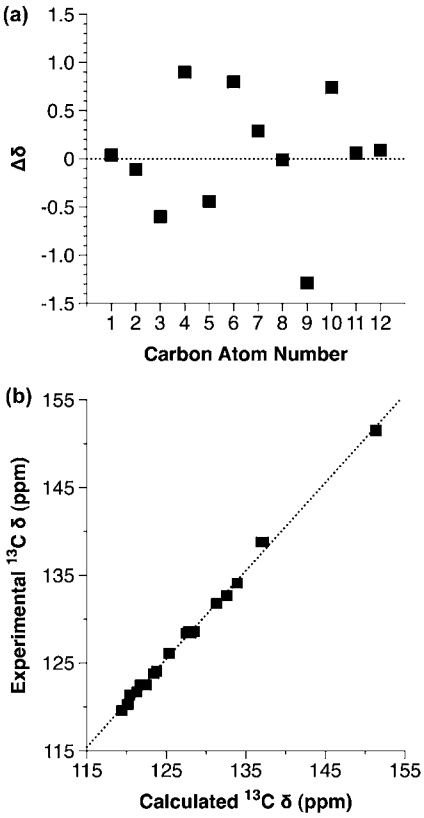

Figure 5. (a) The shift difference ($\Delta\delta$) between the ^{13}C chemical shifts calculated using CASTEP for the two crystallographically-distinct molecules in the (**HBOP**)$_2$ dimer. (b) Plot showing the correlation between the experimental and calculated ^{13}C chemical shifts of **HBOP** in the solid state.

carbons. Although the resolution in the ^{1}H spectrum is not sufficient to distinguish the 18 ^{1}H, which are expected to be present (despite the use of homonuclear ^{1}H decoupling), two distinct groups of ^{1}H resonances are resolved, and cross-sections (taken parallel to δ_2) allow a more accurate estimation of the individual ^{1}H shifts. (It should be noted that the resolution in the ^{1}H MAS spectrum could not be improved even at MAS rates in excess of 60 kHz—see Supplementary data). The information obtained from the two-dimensional spectrum may then be used in an analytical fitting of the ^{13}C MAS spectrum for a more accurate determination of the ^{13}C chemical shifts. Comparison of the experimental values to those calculated by DFT (as shown in Table 2) then allows an assignment of the spectrum. The agreement between calculation and experiment is good, as shown by plot the in Figure 5b, despite the expected poor treatment of dispersion forces (which might be expected to be significant in π-stacked systems) by DFT. Figure 4c shows a ^{13}C MAS NMR spectrum simulated using the calculated ^{13}C chemical shifts (with an inherent linewidth of 80 Hz, determined by fitting one of the resolved resonances in the experimental spectrum), which can be seen to be in good agreement with experiment. It should be noted that in some cases the chemical shifts of the two chemically similar but crystallographically-distinct carbons (i.e., Cx and Cx′) are not resolved in the experiment, e.g., C1/C1′ at δ=151.5 ppm, whereas in some cases distinct splittings are observed, e.g., C9/C9′ (δ=132.9 and 131.8 ppm, respectively). Whilst there is not sufficient resolution in the ^{1}H spectrum to determine accurately the individual shifts to more than ±0.2 ppm, there is broad agreement between the calculated values and the position of the experimental ^{1}H resonances in the two-dimensional correlations experiment, as shown in Table 2.

Figure 6 shows ^{11}B (9.4 T) MAS NMR spectra of **HBOP** in the solid state (both without and with ^{1}H decoupling), acquired using a spin-

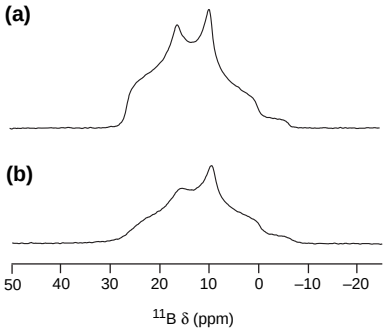

Figure 6. Experimental ^{11}B (9.4 T) MAS NMR spectra of powdered **HBOP** (a) with and (b) without ^{1}H decoupling. Spectra were acquired with a spin-echo pulse sequence (using central-transition selective pulses) to remove the background ^{11}B signal present in the probe. In each case, the MAS rate was 13 kHz.

echo pulse sequence to remove the background ^{11}B signal present in the probe. Although initially the quadrupolar broadened lineshape appears distorted, when decoupling is applied the line can be reasonably well fitted with a single ^{11}B lineshape (C_Q=2.9 MHz, η_Q=0.6 and δ=27 ppm), with little evidence of the two distinct boron sites expected from the crystal structure. The similarity of the two crystallographically-distinct boron sites is confirmed by CASTEP calculations where the two have identical quadrupolar parameters (C_Q=3.3 MHz, η_Q=0.65) and a chemical shift difference of only 0.05 ppm. In comparison to the experiment, the calculation slightly overestimates the magnitude of the quadrupolar coupling, as has been observed[14] for previous ^{17}O, ^{27}Al and ^{25}Mg calculations using CASTEP.

Although 10-hydroxy-10,9-boroxophenanthrene **HBOP** reacts with itself upon heating in the solid state to form the corresponding anhydride **BBE**, in previous work, we were never able to observe this species in solution. However, by rigorous exclusion of water during the preparation of the NMR sample and during the recording of spectra, we established that equilibrium can be driven sufficiently towards the **BBE** in $CDCl_3$ solution to record 1D ^{1}H and ^{13}C spectra and perform a variety of ^{1}H–^{13}C correlation experiments (see Supplementary data). These experiments allowed the complete assignment all of the resonances in the ^{1}H and ^{13}C NMR spectra of **BBE** in solution. As in the case of **HBOP**, this assignment will assist in the interpretation of solid-state data and also provides a test-bed for assessing the quality of DFT calculations of NMR parameters for this compound. The assignment of the resonances observed in the ^{1}H and ^{13}C NMR spectra of **BBE**, recorded in $CDCl_3$ at room temperature, are given in Table 3, together with the numbering system used to identify the individual sites. An overlay of the ^{1}H–^{13}C HSQC spectra of **BBE** and **HBOP** (see Supplementary data) reveals the protons, which experience the largest change in the chemical environment upon the formation of the anhydride **BBE**. Positions 2 and 11 experience the largest changes on moving from **HBOP** to **BBE** and it is the resonances arising from H2 and H11 that show the largest changes in chemical shift. These changes in chemical shift are mirrored by those in the resonances arising from the associated carbon atoms, C2 and C11.

With this assignment in hand, we are in a position to assess the reliability of DFT methods in describing these boroxoaromatic systems. Initially, the ^{13}C NMR parameters for **BBE** were calculated using the CSGT[10] method, as implemented in the Gaussian03[11] suite of programs, the B3LYP functional and a variety of basis sets. Of particular interest was the ability of DFT methods to correctly predict the chemical shifts present in **BBE**, since, from the solid-state structure of **BBE**, it is apparent that the B–O–B bond angle is around 140°, indicating that this structural element has an unusual electronic structure. This unusual bond angle may result in the

Table 3
Assignment of the resonances observed in the ^{1}H and ^{13}C NMR spectra of **BBE** recorded in CDCl3 at room temperature and the chemical shifts calculated using the CSGT method at the B3LYP 6-311++G(2d,p) level of theory

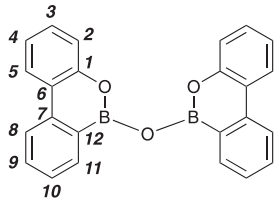

Assignment	Calculated[a]		Experimental	
	^{13}C (Non-planar) (ppm)	^{13}C (Planar)(ppm)	^{13}C (ppm)	^{1}H (ppm)
1	154.7	155.1	151.4	—
2	120.5	121.2	120.2	7.29
3	129.6	129.9	129.2	7.33
4	122.3	122.9	123.0	7.20
5	123.9	124.1	123.6	8.13
6	124.8	124.9	123.1	—
7	143.4	144.2	141.7	—
8	121.5	122.2	121.7	8.16
9	133.6	133.8	133.0	7.68
10	127.0	127.3	127.3	7.39
11	136.3	136.5	134.3	8.07
12	124.9	125.6	—[b]	—

[a] Planar and non-planar refer to the relative orientations of the two boroxoaromatic rings in **BBE**. Planar represents the solid-state structure (angle=0°). Non-planar represents the local minimum geometry located at the B3LYP/6-311++G(2d,p) level of theory (angle=28.7°).

[b] The resonance arising from C12 cannot be detected in the 1D ^{13}C spectrum as a result of the fast T2 relaxation of the bonded quadrupolar ^{11}B/^{10}B (I=3/2 and I=3, respectively).

propagation of differences in electronic structure across the π system. Another issue is the question of the solution-state structure of **BBE**. In the solid state, the **BBE** molecule must be planar to satisfy packing constraints. However, in solution, no such constraints exist and, presumably, the ^{1}H and ^{13}C spectra are fast exchange averages of the spectra from a series of low energy conformations. In an attempt to account for this conformational averaging, we compared the chemical shifts calculated for **BBE** with a planar conformation with those calculated using an energy minimum structure located at the B3LYP/6-311++G(2d,p) level of theory. In this non-planar structure, the planes of the two boroxoaromatic systems are at an angle of 28.7° with respect to each other. This conformation is only 1.8 kcal more stable than the planar conformation. As before, the calculation of the magnetic shieldings was performed using the CSGT method at the B3LYP/6-311++G(2d,p) level of theory and the results are summarized in Table 3.

The ^{13}C chemical shifts calculated at this level of theory for both the planar **BBE** (Fig. 7a) and the corresponding non-planar conformation (Fig. 7b) show excellent correlations with the experimental solution phase data. The fact that both the planar and the non-planar structures correlate very well and with comparable quality to the experimental set of resonances suggests that both are reasonable representations of the average structure of **BBE** in $CDCl_3$ solution at room temperature. The largest deviations between the experimental chemical shifts and the calculated chemical shifts for both the non-planar and planar **BBE** are associated with the quaternary carbons atoms, in particular C1, mirroring the pattern of deviations observed for **HBOP**.

The ^{13}C MAS NMR spectrum of powdered **BBE**, shown in Figure 8a, is broadly similar to that of solid-state **HBOP**, exhibiting a range of resonances between 115 and 155 ppm. The quaternary carbons can once again be identified through the use of dipolar dephasing experiments, as shown in Figure 8b, with δ=151.5, 140.8, 126.4 and 123.0 ppm. The much broader resonance at 126.4 ppm

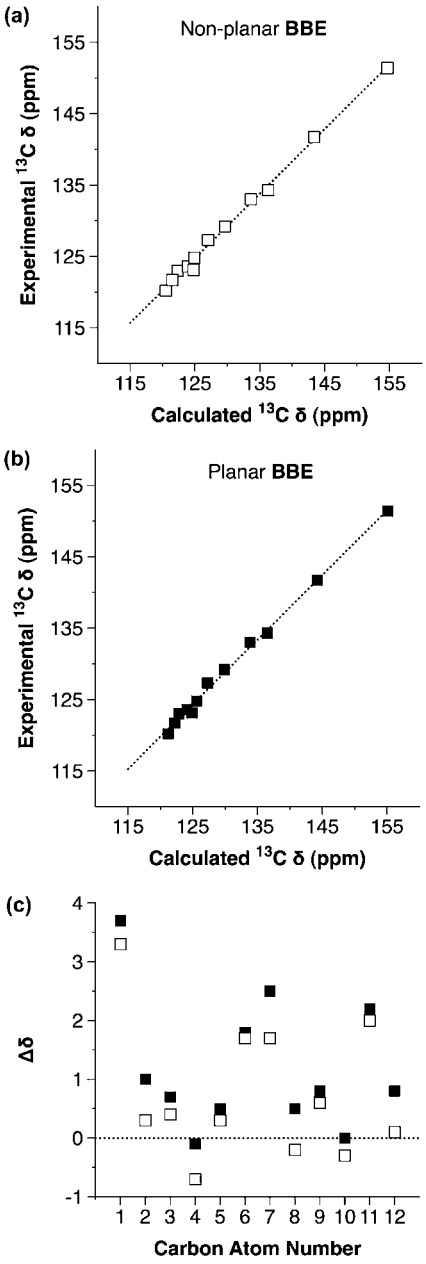

Figure 7. (a) Correlation between the experimental ^{13}C chemical shifts and those calculated for the non-planar **BBE** molecule using the CSGT method at the B3LYP/6-311++G(2d,p) level of theory. (b) Correlation between the experimental ^{13}C chemical shifts and those calculated for the planar **BBE** molecule using the CSGT method at the B3LYP 6-311++G(2d,p) level of theory. (c) Signed differences ($\Delta\delta$) in the ^{13}C chemical shifts for the non-planar **BBE** molecule (open squares) and the planar **BBE** molecule (filled squares) compared to the chemical shifts observed experimentally for **BBE** in $CDCl_3$ solution at room temperature.

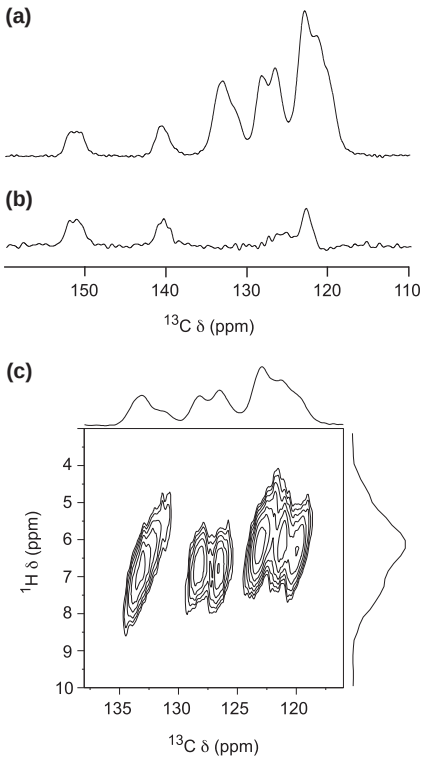

Figure 8. Experimental ^{13}C (9.4 T) (a) MAS and (b) dipolar dephasing MAS NMR spectra of powdered **BBE**. In each case, spectra were recorded using ramped cross polarization with a contact pulse of 1 ms and with SPINAL64 heteronuclear ^{1}H decoupling. In (b), there was an (undecoupled) interval of 60 μs after the cross-polarization step and prior to the formation of a ^{13}C spin echo (where ^{1}H decoupling was applied), during which the resonances corresponding to ^{13}C species with attached ^{1}H were dephased. The MAS rates were (a) 12 kHz and (b) 6 kHz. (c) Two-dimensional ^{1}H/^{13}C (11.7 T) HETCOR correlation spectrum of solid **BBE**, with homonuclear FSLG ^{1}H decoupling in the indirect dimension and SPINAL64 heteronuclear ^{1}H decoupling in acquisition. The contact time in the cross polarization step was 100 μs. The MAS rate was 13 kHz.

corresponds to C12, which is directly bonded to ^{10}B/^{11}B, and broadened by the associated scalar couplings. Notably, the resonance with δ of 140.8 ppm, identified, at least initially, by comparison to **HBOP** as *C*7, exhibits a significant shift (of ~2 ppm) in the **BBE** spectrum, whilst those for the remaining quaternary carbons are much less affected. However, in contrast to the **HBOP** spectrum, the peaks appear much broader for **BBE**, for example, the resonance at δ=151.5 ppm (thought to be C1 by comparison with **HBOP**) is over 3.5 times broader than the corresponding peak in Figure 4a, and appears to be composed of a number of overlapping resonances. This can also be seen in the ^{1}H/^{13}C two-dimensional HETCOR spectrum shown in Figure 8c, where the resonances (all non-quaternary carbons) appear to exhibit a distribution of chemical shifts in both dimensions.

Although the solid-state structure of **HBOP** is well known, there has been disagreement over the detailed structure of **BBE** in the solid state. Initial work[15] by Sheldrick et al., using single crystals prepared by sublimation, proposed a monoclinic unit cell (β=99.64°), with the **BBE** molecules aligning along the z axis to promote favourable π-stacking interactions. The structure was refined using space group $P2_1/c$, with the exact orientation of the B–O–B bridge not able to be accurately determined, i.e., a structure where there is disorder in both the position of the central oxygen species (split between two distinct sites with 50% occupancy) and in the nature of the atoms in the heterocyclic ring. The two positions of the central oxygen species correspond to two different orientations of the **BBE** molecules, such that all atomic positions, except these oxygens, are identical irrespective of atom type. In contrast, our later work[4] studied, using powder X-ray diffraction, **BBE** produced directly by solid-state reaction of **HBOP**. In addition to the disordered $P2_1/c$ model described above, this work also considered a second structure (refined in space group $P2_1$), where the orientation of the B–O–B bridge was ordered, resulting in two crystallographically-distinct **BBE** molecules in the unit cell. From the PXRD Rietveld refinement it was not possible to distinguish between the two models, with each giving equally good fits to the experimental data. The degree of order present for **BBE** materials may, of course, depend upon the preparation method. There is no

reason to suppose that crystals formed by heating **HBOP**, i.e., a solid-state reaction within the confines of a crystal lattice, will necessarily produce exactly the same structure as that when **HBOP** is melted. In addition, the different techniques used in the analysis may also affect the accuracy and completeness of the information produced. For example, single-crystal X-ray diffraction is expected to accurately identify the atomic positions; however, unless a large number of crystals are sampled, it does not provide detailed information on the nature of the bulk material. In contrast, PXRD does contain information on the bulk material, and on all of the phases and impurities, which may be present, but the accuracy with which detailed information (such as exact atomic coordinates) can be extracted is more limited. For the case of **BBE**, as shown[4] by our work, PXRD is unable to distinguish between two different structures, one of which is ordered, the second disordered.

The solid-state MAS spectra of **BBE** shown in Figure 8 support the presence of a degree of disorder, exhibiting broadened peaks with apparent distributions of chemical shifts. The sample used in this work was prepared by heating **HBOP** at 90 °C for 6 h, i.e., a direct solid state transformation as in our work.[4,16] However, ^{13}C NMR spectra of materials prepared from melted **HBOP** (both cooled slowly and rapidly), were also very similar, although not identical, both to each other and to the original sample (see Supplementary data), indicating the presence of some structural disorder in all materials. For disordered materials the NMR spectrum should consist of a sum of resonances resulting from all possible local environments. In order to investigate the range of shifts this would produce in **BBE**, planewave DFT calculations were carried out for the structural models shown in Figure 9. All models exhibit some form of long-range order (owing to the periodic nature of the calculation) but should provide information on a variety of local environment types. The structures in Figures 9a and **9b** contain **BBE** molecules stacked along the *z* axis such that all B–O–B bridges point in the same direction. Figure 9b corresponds to the $P2_1$ model refined by Greig et al., whilst Figure 9a shows a similar structure where the relative orientation of the B–O–B bonds between the two sets of π-stacks is different. In contrast, Figure 9c shows a (1×1×2) supercell, where the orientation of the B–O–B bridges alternates within a series of π-stacked **BBE** molecules.

The ^{13}C chemical shifts calculated for the three different models are shown, for each distinct C species, in Figure 10, with green, red and blue points representing the values calculated for the structures in Figures 9a, **9b** and **9c**, respectively. A range of chemical shifts is observed for each distinct C species, from ~0.5 ppm for C10 to ~3.5 ppm for C9. The chemical shifts calculated for the structures in Figures 9a and **9b** are generally similar, demonstrating that longer range changes (i.e., changes in the other set of π-stacked molecules) have relatively little effect. In contrast, a much greater spread of shifts is found for the supercell in Figure 9c, where there are more significant changes in the local environment, with B–O–B bridges that alternate, rather than align, in orientation within a π-stack. In general, the spread of calculated chemical shifts in Figure 10 is in good agreement with the linewidths found experimentally. This effect is perhaps more easily seen in Figure 11, where simulated ^{13}C MAS NMR spectra are shown (using an inherent linewidth of 80 Hz) for the chemical shifts calculated for the three structures in Figure 9. In addition, Figure 11d shows the spectrum, which would result when the three spectra are added together (modelling the range of environments found in a disordered material). All spectra are consistent with that observed experimentally, suggesting that the experimental linebroadening does result from structural disorder; more specifically a disorder in the nature of the atoms in the heterocyclic ring and the orientation of the B–O–B bridge between different **BBE** molecules.

Figure 12 shows ^{11}B (9.4 T) MAS NMR spectra of **BBE** in the solid state (both with and without ^{1}H decoupling), acquired using a spin-

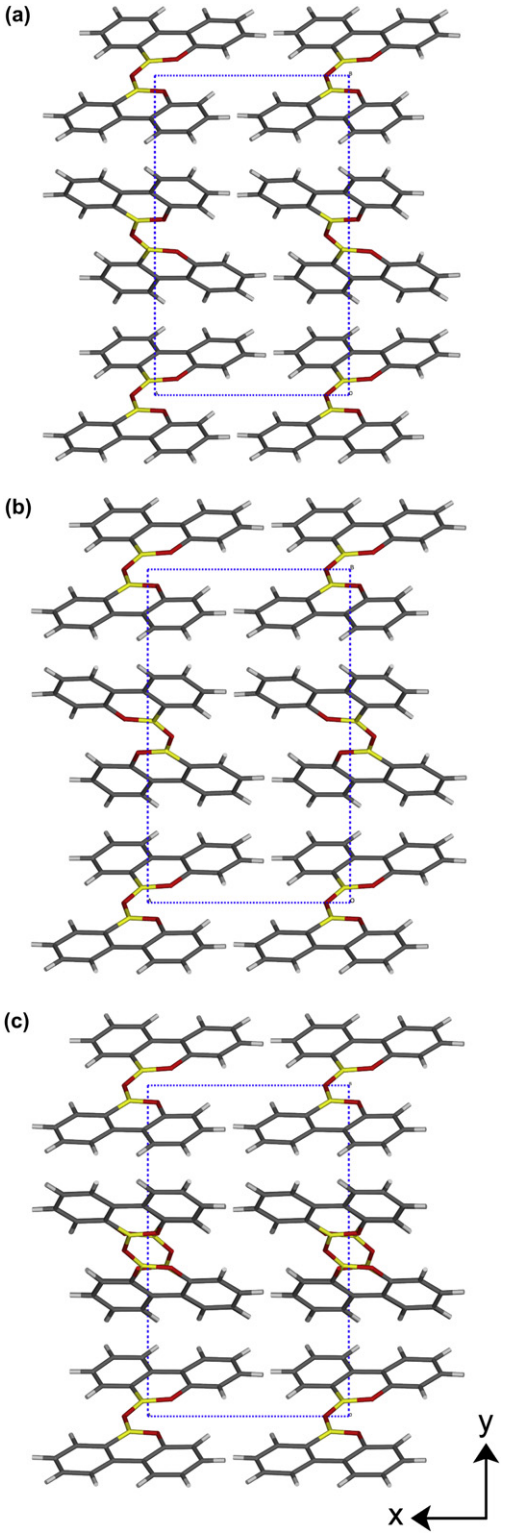

Figure 9. A view looking down the z axis of the structural models of **BBE** used to calculate ^{13}C NMR parameters. The structure in (c) is a (1×1×2) supercell where the orientation of the B–O–B bridges in one set of π-stacked molecules alternates along the z axis. Carbon, hydrogen, boron and oxygen atoms are shown in dark grey, light grey, yellow and red, respectively. The unit cell is shown by dashed blue lines.

echo pulse sequence. In contrast to the spectra of **HBOP** in Figure 6, decoupling has a less significant effect on the signal intensity and lineshape, owing presumably, to the removal of the directly bonded OH species in the anhydride. The spectrum can be fitted well using

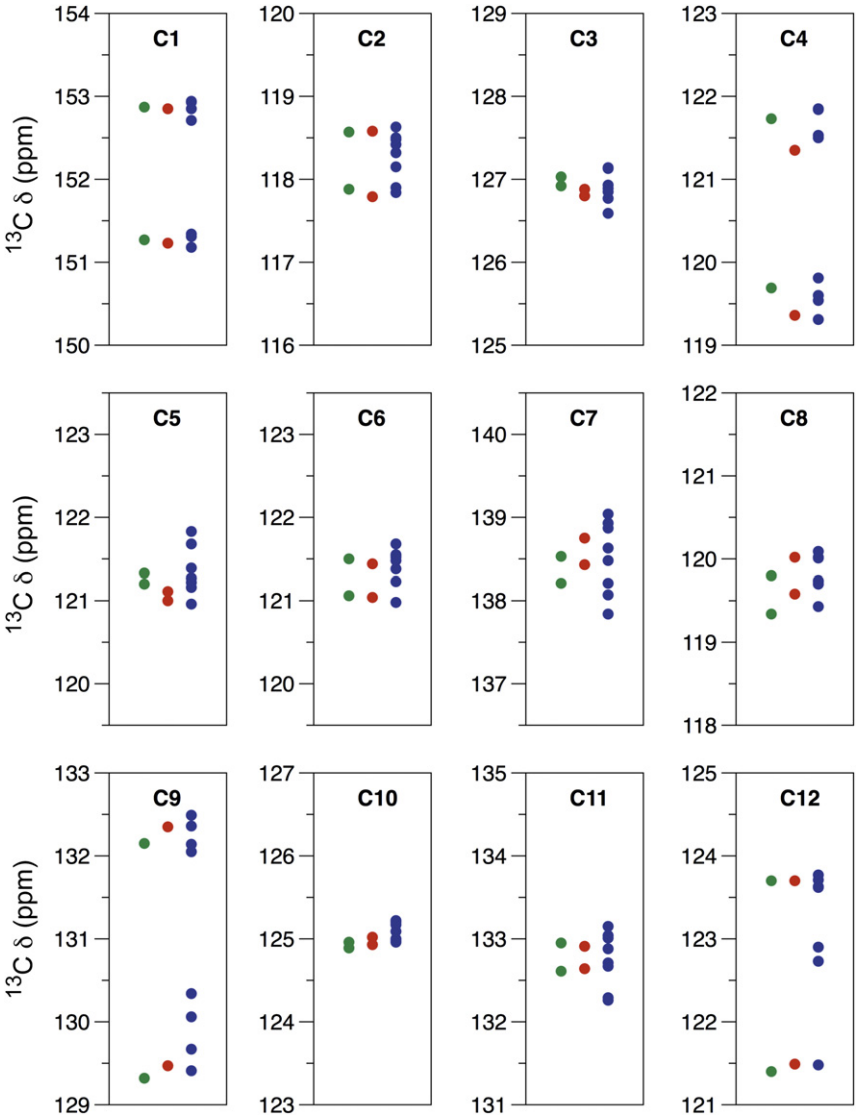

Figure 10. Calculated (using CASTEP) ^{13}C chemical shifts for each of the distinct C species for the structural models shown in Figure 9a (green circles), Figure 9b (red circles) and Figure 9c (blue circles).

a single ^{11}B lineshape, with similar, but not identical, parameters (C_Q=2.9 MHz, η_Q=0.5 and δ=25 ppm) to **HBOP**. The ^{11}B NMR parameters calculated for the three structural models shown in Figure 9, however, are all very similar, with C_Q=3.3 MHz, η_Q=0.54 and a range of chemical shifts of less than 0.3 ppm, demonstrating that ^{11}B NMR cannot be used to distinguish the different structures of solid-state **BBE**. A distinction can be made however, between **BBE** and **HBOP**, as although C_Q values are very similar there is a distinct change in η_Q (of ~0.1) and a significant chemical shift (of ~2 ppm).

The presence of the second-order quadrupolar broadening in the ^{11}B spectra of **HBOP** and **BBE** shown in Figures 6 and **12**, whilst providing some information on local symmetry and structure, does hinder resolution. A high-resolution spectrum, free from quadrupolar broadening, can be obtained from a projection (onto δ_1) of a two-dimensional MQMAS spectrum, as shown in Figure 13. Despite the removal of the quadrupolar broadening, the two crystallographically-distinct species in **HBOP** still cannot be resolved as a result of the similarity of their local environments, as shown in Figure 13a. A single resonance is also observed for **BBE** (Fig. 13c), but with a different isotropic shift to that of **HBOP**, demonstrating that mixtures of the two species can be distinguished and quantified in this way. Interestingly, the spectrum of **HBOP** heated at only 50 °C (Fig. 13b), a temperature at which we had previously been unable to detect any solid-state reaction by PXRD, does indicate that a small amount of **BBE** is present within the sample. This observation suggests that the transformation of two **HBOP** molecules to one molecule of **BBE** is, in fact, associated with a much lower activation barrier than that derived previously from PXRD or TGA data. As noted earlier, the observed rate of transformation using these techniques may, in fact, be a function of the rate of water loss and lattice reorganization.

In order to investigate this hypothesis further, we turned once again to computation. Although it is possible to use planewave DFT methods and periodic boundary conditions to model reactivity in the solid state, the imposition of these conditions on a single unit cell would force the transformation of **HBOP** to **BBE** at all points in the lattice simultaneously. A concerted transformation of this type is physically unreasonable. In addition, the computational cost for creating a supercell in which only one dimer was transformed is prohibitive. Therefore, calculations performed on an isolated cluster of the crystal lattice is much more desirable as the formation of a single molecule of **BBE** within this cluster can be investigated. In order to perform such calculations, a compromise must be adopted.

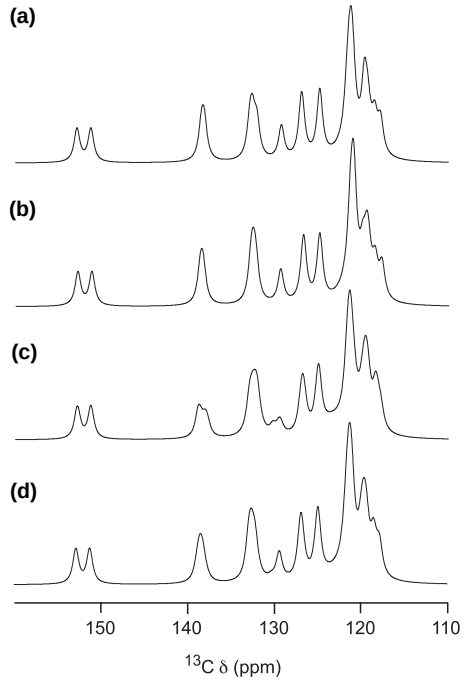

Figure 11. ^{13}C (9.4 T) MAS NMR spectra simulated with the (CASTEP) calculated ^{13}C chemical shifts for the structural models of **BBE** shown in (a) Figure 9a, (b) Figure 9b, (c) Figure 9c. In (d), the summation of the spectra in (a), (b) and (c) is shown. For most resonances an inherent linewidth of 80 Hz was assumed, whilst for C12 (directly bonded to ^{10}B/^{11}B) a larger linewidth of 280 Hz was employed.

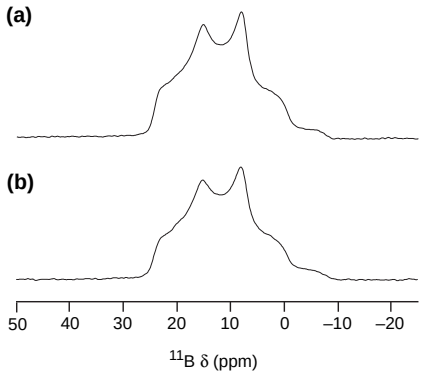

Figure 12. Experimental ^{11}B (9.4 T) MAS NMR spectra of powdered **BBE** (a) with and (b) without ^{1}H decoupling. Spectra were acquired with a spin-echo pulse sequence (using central-transition selective pulses) to remove the background ^{11}B signal present in the probe. In each case, the MAS rate was 13 kHz.

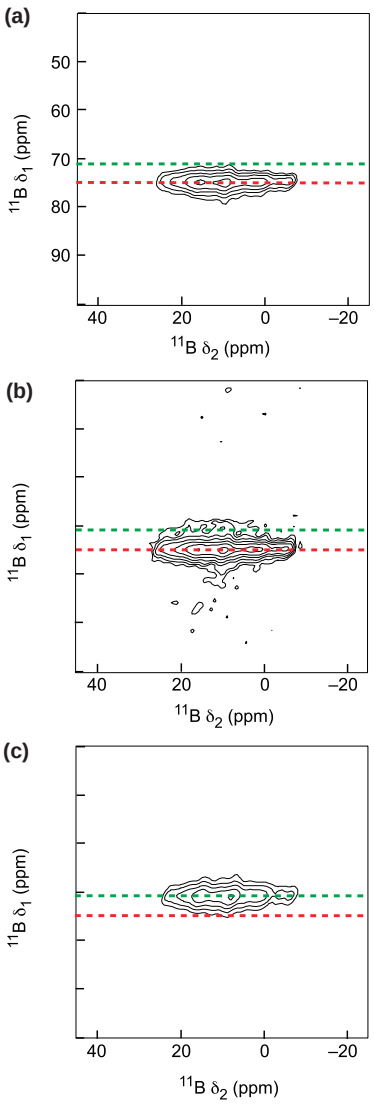

Figure 13. Experimental ^{11}B (9.4 T) triple-quantum MAS NMR spectra, of (a) **HBOP**, (b) **HBOP** heated at 50 °C for 24 h and (c) **BBE**, recorded using a phase-modulated split-t_1 shifted echo pulse sequence, with ^{1}H decoupling. In each case, the MAS rate was 12.5 kHz. The red and green lines are added to guide the eye.

Within the crystal lattice, the transformation from **HBOP** to **BBE** occurs between two π-stacked hydrogen-bonded **HBOP** dimers. In order to simulate the packing of the crystal lattice around this reacting pair of dimers, it is necessary (Fig. 14a) to use a cluster of 20 **HBOP** molecules arranged in 10 hydrogen-bonded dimers. Ideally, we would wish to perform these calculations using DFT, however, this approach is, again, too expensive computationally on a system of this size (300 heavy atoms) and, therefore, we decided to explore the solid-state transformation using the PM6[17] semi-empirical method.

Our starting point was a cluster of 20 **HBOP** molecules arranged in 10 hydrogen-bonded dimers (Fig. 14a). In the first calculation, the length of the B–O vector marked in purple (Fig. 14b) was shortened progressively leading to the formation of a new local minimum structure (Fig. 14c) in which two B–O covalent bonds have been formed. The four hydrogen bonds present in the starting structure are still present at this point. Transfer of a proton from one O atom of the four-membered ring to the other leads to spontaneous breaking of one of the B–O bonds, leading to the formation of a new local minimum structure (Fig. 14d) in which a water molecule is coordinated to one of the boron atoms of a newly formed molecule of **BBE**. Two of the four original hydrogen bonds are preserved in this new structure. Lengthening of the bond between the boron atom of the **BBE** molecules and the oxygen atom of the water molecule leads to dissociation of the water molecule and some reorganization of the local structure (Fig. 14e). In particular, the water molecule moves slightly within the pocket it occupies within the cluster to form a hydrogen bond with the hydroxyl group of the adjacent **HBOP** molecule, that is, no longer part of an (**HBOP**)$_2$ dimer. As expected, the **BBE** molecule undergoes rehybridisation at both boron and at its bridging oxygen atom as a result of the dissociation of the water molecule. The most striking feature of this entire set of reactions is that there is little or no perturbation of the surrounding cluster during the entire process. Extrapolating from these observations to the solid state, these results suggest that it is, indeed, possible for **HBOP** to react to form **BBE** within the crystal

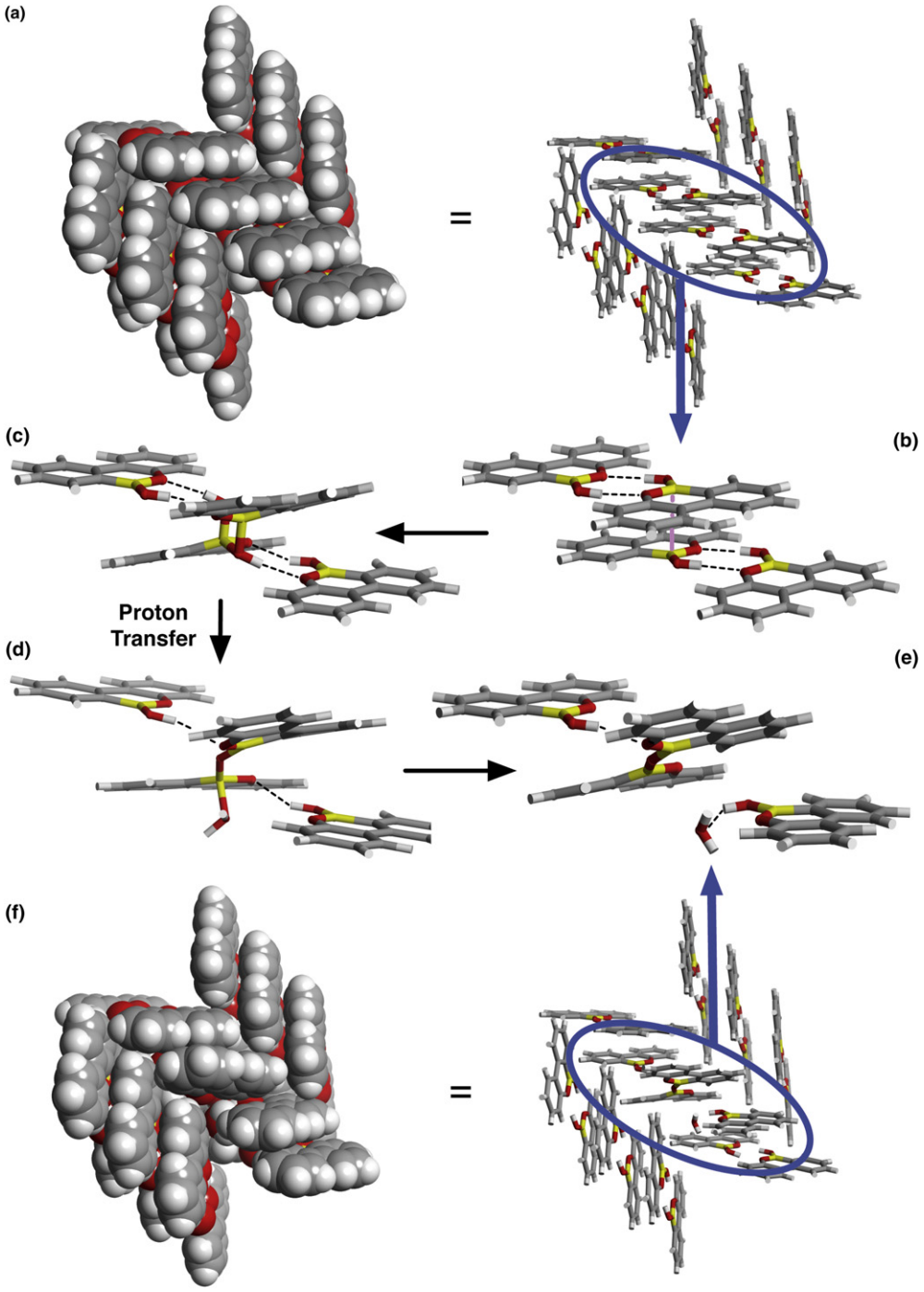

Figure 14. Computational mapping of the transformation of **HBOP** to **BBE** within the crystal lattice. (a) CPK (left) and tube (right) representations of the cluster of 10 **HBOP** hydrogen-bonded dimers used in the PM6 semi-empirical calculation of the transformation pathway for **HBOP** to **BBE**. The two hydrogen-bonded **HBOP** dimers that react are in the centre of the cluster and are highlighted in blue. For clarity, in representations (b)→(e), only the molecules undergoing transformation are shown, although the PM6 calculation included the entire cluster. (b) Starting point for mapping the reaction pathway. In the calculation, the length of the B–O vector marked in purple was shortened leading to intermediate (c). Transfer of a proton affords intermediate (d) that contains two **HBOP** molecules and a molecule of **BBE**, which has a water molecule coordinated to one of its B atoms. (e) Dissociation of intermediate (d) affords two **HBOP** molecules, a molecule of **BBE** and a water molecule within the crystal lattice. (f) CPK (left) and tube (right) representations of the cluster after the transformation of **HBOP** to **BBE**. The transformation causes minimal disruption of the packing within the cluster of **HBOP** molecules. In all cases, carbon atoms are coloured grey, boron atoms are coloured yellow, oxygen atoms are coloured red and hydrogen atoms are coloured light grey. Hydrogen bonds are indicated by dashed lines.

lattice at relatively low temperatures. This observation is consistent with the fact that **HBOP** reacts[3e,4,16] extremely rapidly, even at −40 °C, in $CDCl_3$ solution with oxygen nucleophiles.

The **BBE**, that is, formed in the process depicted in Figure 14 is in a different conformation to that observed in the solid-state structure of **BBE**. Secondly, the dissociation of the water molecule (Fig. 14d→Fig. 14e) is predicted to be significantly endothermic, at least at the PM6 level of theory. This observation would suggest that a mechanism must be present for transporting the water away from the site of reaction in order for the reaction to progress towards complete conversion of **HBOP** to **BBE**. It would therefore seem likely that it is the conformational reorganization of **BBE** and the loss of water that are likely to be the rate limiting factors in this solid-state transformation.

3. Conclusions

In this work, we have demonstrated that solid-state NMR spectroscopy, coupled with calculation, can expose and rationalize subtleties in a solid-state reaction that both diffraction and gravimetric analysis are incapable of detecting. We have shown that DFT calculations, both for isolated molecules and in periodic systems, provide a level of accuracy, that is, sufficient to facilitate the assignment of ^{13}C NMR spectra in solution and in the solid state, even when considerable spectral overlap is present. This combined approach has exposed significant limitations in our previous methods of probing reactivity of boron-containing heteroaromatic systems in the solid state, which relied on diffraction and gravimetric analysis. In particular, for samples with thermal histories that diffraction cannot detect any reaction, high resolution ^{11}B solid-state NMR spectra have allowed us to detect the signature of solid-state reactivity, even at very low levels. These results indicate that solid-state NMR spectroscopy is capable of detecting isolated pockets of reaction within a crystal, in contrast to diffraction, which requires the presence of long-range order. Since calculations reveal that the transformation 2 (**HBOP**)$_2$ → **BBE**+2**HBOP**+H_2O is possible at isolated points in the crystal lattice with minimal distortion of the local structure, it seems likely that it is these isolated reaction events that are being detected by NMR. Additionally, we have demonstrated that solid-state NMR, in combination with first principles calculations, can detect disorder in **BBE**, irrespective of the method of synthesis—a task that diffraction finds difficult. Current work in our laboratory is focussed on acquiring time-resolved data for this type of transformation using NMR. The approach described here may find significant utility in probing reactions in the solid state that cannot be studied easily by more traditional methods.

4. Experimental

4.1. General

Solid-state NMR spectra were acquired using Bruker Avance consoles equipped with either 9.4, 11.7 or 14.1 T wide-bore magnets. Powdered samples were packed in conventional 4-mm ZrO_2 rotors and rotated at rates between 6 and 14 kHz. Chemical shifts are shown relative to TMS for ^{13}C and ^{1}H (using alanine as a secondary reference), and to $BF_3{\cdot}Et_2O$ in $CDCl_3$ for ^{11}B (using BPO_4 as a secondary reference). For ^{13}C, spectra were acquired using cross-polarization with a ramped spin-lock pulse for ^{1}H and contact times between 0.1 and 2 ms. Heteronuclear ^{1}H decoupling (typically using SPINAL64[18]) was applied in acquisition. Typical recycle intervals were 10 s. For ^{11}B, spectra were acquired using a spin-echo pulse sequence to minimise the background contributions from the probe. In some cases heteronuclear CW ^{1}H decoupling was applied in acquisition. Typical recycle intervals were 2 s. For MQMAS experiments spectra were acquired using a phase-modulated split-t_1 shifted-echo sequence with heteronuclear CW ^{1}H decoupling.[19] The scale of the isotropic axis was plotted according to the convention in Ref. 20.

Planewave DFT calculations were carried out using the CASTEP code, employing the gauge included projector augmented wave[12b] (GIPAW) algorithm to reconstruct the all-electron wavefunction in a magnetic field. The generalized gradient (GGA) PBE functional was used and core-valence interactions described by ultrasoft pseudopotentials.[21] Integrals over the Brilloiun zone were performed using a Monkhurst-Pack grid with a k-point spacing of 0.05 $Å^{-1}$. Wavefunctions were expanded in planewaves with a kinetic energy smaller than a cut-off energy, typically 600–700 eV. The absolute shielding tensor and electric field gradient (EFG) tensor were generated in the crystal frame. From this the isotropic chemical shift, δ, is given by $-(\sigma-\sigma_{ref})$, with reference shieldings of 193.99 ppm and 29.11 ppm used for ^{13}C and ^{1}H, respectively. The magnitude (C_Q) and asymmetry (η_Q) of the quadrupolar interaction are given by $C_Q=eQV_{ZZ}/h$ and $\eta_Q=(V_{XX}-V_{YY})/V_{ZZ}$. A quadrupole moment, eQ, of 40.59 mB was used for ^{11}B. Where necessary, geometry optimization of structures was also performed within CASTEP. Calculations were performed using the EaStCHEM Research Computing Facility, which consists of 136 AMD Opteron processing cores partly connected by Infinipath high speed interconnects.

NMR parameters for **HBOP** and **BBE** as single molecules (or hydrogen-bonded dimers) were calculated using Gaussian03 (Revision D.01). Initially, the molecular structure was optimised at the HF/6-31 G level of theory. These structures were then used as the input for DFT calculations (B3LYP/6-311++G(2d,p)). After optimisation of the molecular structure using DFT, NMR parameters were calculated using the CSGT method and B3LYP/6-311++G(2d,p). ^{1}H and ^{13}C chemical shifts were referenced to benzene, whose NMR parameters were calculated at the same level of theory. All calculations were performed using the EaStCHEM Research Computing Facility.

Semi-empirical calculations were carried out using the MOPAC2009[22] semi-empirical code (Version 9.302L), running on a 64-bit CentOS 5 Linux platform, was used for all calculations. The initial input geometry for the cluster of 20 **HBOP** molecules was created from our published single-crystal X-ray structure of **HBOP**. Reaction coordinates were driven using the POINT and STEP keywords in MOPAC—the step size was 0.05 Å in all cases. Intermediate and final structures were minimized using eigenvector following (EF) to gradient norms less than 2.00.

Acknowledgements

We thank EaStCHEM for the award of a postgraduate studentship to DC. This work was supported by the Engineering and Physical Sciences Research Council in the UK (Grant EP/E041825/1). We thank Dr. Robin Orr and Dr. Melinda Duer (University of Cambridge) and Dr. Stefan Steuernagel (Bruker Biospin, Germany) for access to solid-state NMR facilities.

Supplementary data

Supplementary data associated with this article can be found in the online version at doi:10.1016/j.tet.2010.05.065. These data include MOL files and InChIKeys of the most important compounds described in this article.

References and notes

1. (a) Desiraju, G. R. *Angew. Chem., Int. Ed. Engl.* **1995**, *34*, 2311; (b) Aakeröy, C. B.; Salmon, D. J. *CrystEngComm* **2005**, 439; (c) Örn, A.; Zaworotko, M. J. *Chem. Commun.* **2004**, 1889; (d) Aoyama, Y.; Endo, K.; Anzai, T.; Yamaguchi, Y.; Sawaki, T.; Kobayashi, K.; Kanehisa, N.; Hashimoto, H.; Kai, Y.; Masuda, Y. *J. Am. Chem. Soc.* **1996**, *118*, 5562.
2. (a) Braga, D.; Grepioni, F. *Angew. Chem., Int. Ed.* **2004**, *43*, 4002; (b) Garcia-Garibay, M. A. *Acc. Chem. Res.* **2003**, *36*, 491; (c) Scheffer, J. R.; Xia, W. *Top. Curr. Chem.* **2005**, *254*, 233; (d) Kaupp, G. *CrystEngComm* **2003**, *5*, 117; (e) MacGillivray, L. R.; Papaefstathiou, G. S.; Friščić, T.; Hamilton, T. D.; Bučar, D.-K.; Chu, Q.; Varshney, D. B.; Georgiev, I. G. *Acc. Chem. Res.* **2008**, *41*, 280; (f) MacGillivray, L. R. *J. Org. Chem.* **2008**, *73*, 3311; (g) Friščić, T.; Hamilton, T. D.; Papaefstathiou, G. S.; MacGillivray, L. R. *J. Chem. Educ.* **2005**, *82*, 1679; (h) Gao, X.; Friščić, T.; MacGillivray, L. R. *Angew. Chem., Int. Ed.* **2004**, *43*, 232; (i) Georgiev, I. G.; MacGillivray, L. R. *Chem. Soc. Rev.* **2007**, 1239; (j) Vittal, J. J. *Coord. Chem. Rev.* **2007**, *251*, 1781; (k) Enkelmann, V.; Wegner, G.; Novak, K.; Wagener, K. B. *J. Am. Chem. Soc.* **1993**, *115*, 10390; (l) Takahashi, S.; Miura, H.; Kasai, H.; Okada, S.; Oikawa, H.; Nakanishi, H. *J. Am. Chem. Soc.* **2002**, *124*, 10944; (m) Bučar, D.-K.; MacGillivray, L. R. *J. Am. Chem. Soc.* **2007**, *129*, 32.
3. (a) Harris, K. D. M.; Kariuki, B. M.; Lambropoulos, C.; Philp, D.; Robinson, J. M. A. *Tetrahedron* **1997**, *53*, 8599; (b) Robinson, J. M. A.; Kariuki, B. M.; Philp, D.; Harris, K. D. M. *Tetrahedron Lett.* **1997**, *38*, 6281; (c) Comina, P. J.; Philp, D.; Kariuki, B. M.; Harris, K. D. M. *Chem. Commun.* **1999**, 2279; (d) Robinson, J. M. A.; Philp, D.; Kariuki, B. M.; Harris, K. D. M. *J. Chem. Soc., Perkin Trans. 2* **2001**, 2166; (e) Greig, L. M.; Slawin, A. M. Z.; Smith, M. H.; Philp, D. *Tetrahedron* **2007**, *63*, 2391.
4. Greig, L. M.; Kariuki, B. M.; Habershon, S.; Spencer, N.; Johnston, R. L.; Harris, K. D. M.; Philp, D. *New J. Chem.* **2002**, *26*, 701.

5. Brown, W. E.; Dollimore, D.; Galwey, A. K. In *Comprehensive Chemical Kinetics*; Bamford, C. H., Tipper, C. F. H., Eds.; Elsevier Scientific Publishing: Oxford, 1980; p 57.
6. (a) Turega, S. M.; Philp, D. *Chem. Commun.* **2006**, 3684; (b) Bennes, R. M.; Philp, D. *Org. Lett.* **2006**, *8*, 3651; (c) Cowie, R. M.; Turega, S. M.; Philp, D. *Org. Lett.* **2006**, *8*, 5179; (d) Pearson, R. J.; Kassiandis, E.; Slawin, A. M. Z.; Philp, D. *Chem.—Eur. J.* **2006**, *12*, 6829; (e) Kassiandis, E.; Philp, D. *Angew. Chem., Int. Ed.* **2006**, *45*, 6344; (f) Kassiandis, E.; Pearson, R. J.; Philp, D. *Chem.—Eur. J.* **2006**, *12*, 8788; (g) Jones, C. E. S.; Turega, S. M.; Clarke, M. L.; Philp, D. *Tetrahedron Lett.* **2008**, *49*, 4666; (h) Sinclair, A. J.; del Amo, V.; Philp, D. *Org. Biomol. Chem.* **2009**, *7*, 3308; (i) del Amo, V.; Philp, D. *Org. Lett.* **2009**, *11*, 301.
7. Stahl, I.; von Kiedrowski, G. *J. Am. Chem. Soc.* **2006**, *128*, 14014.
8. Andrew, E. R.; Bradbury, A.; Eades, R. G. *Nature* **1958**, *182*, 1659.
9. Frydman, L.; Harwood, J. S. *J. Am. Chem. Soc.* **1995**, *117*, 5367.
10. (a) Keith, T. A.; Bader, R. F. W. *Chem. Phys. Lett.* **1992**, *194*, 1; (b) Keith, T. A.; Bader, R. F. W. *Chem. Phys. Lett.* **1993**, *210*, 223; (c) Cheeseman, J. R.; Trucks, G. W.; Keith, T. A.; Frisch, M. J. *J. Chem. Phys.* **1996**, *104*, 5497.
11. Frisch, M. J.; Trucks, G. W.; Schlegel, H. B.; Scuseria, G. E.; Robb, M. A.; Cheeseman, J. R.; Montgomery, J. A., Jr.; Vreven, T.; Kudin, K. N.; Burant, J. C.; Millam, J. M.; Iyengar, S. S.; Tomasi, J.; Barone, V.; Mennucci, B.; Cossi, M.; Scalmani, G.; Rega, N.; Petersson, G. A.; Nakatsuji, H.; Hada, M.; Ehara, M.; Toyota, K.; Fukuda, R.; Hasegawa, J.; Ishida, M.; Nakajima, T.; Honda, Y.; Kitao, O.; Nakai, H.; Klene, M.; Li, X.; Knox, J. E.; Hratchian, H. P.; Cross, J. B.; Bakken, V.; Adamo, C.; Jaramillo, J.; Gomperts, R.; Stratmann, R. E.; Yazyev, O.; Austin, A. J.; Cammi, R.; Pomelli, C.; Ochterski, J. W.; Ayala, P. Y.; Morokuma, K.; Voth, G. A.; Salvador, P.; Dannenberg, J. J.; Zakrzewski, V. G.; Dapprich, S.; Daniels, A. D.; Strain, M. C.; Farkas, O.; Malick, D. K.; Rabuck, A. D.; Raghavachari, K.; Foresman, J. B.; Ortiz, J. V.; Cui, Q.; Baboul, A. G.; Clifford, S.; Cioslowski, J.; Stefanov, B. B.; Liu, G.; Liashenko, A.; Piskorz, P.; Komaromi, I.; Martin, R. L.; Fox, D. J.; Keith, T.; Al-Laham, M. A.; Peng, C. Y.; Nanayakkara, A.; Challacombe, M.; Gill, P. M. W.; Johnson, B.; Chen, W.; Wong, M. W.; Gonzalez, C.; Pople, J. A. *Gaussian 03, Revision D.01*; Gaussian: Wallingford CT, 2004.
12. (a) Seagall, M. D.; Lindan, P. J. D.; Probert, M. J.; Pickard, C. J.; Hasnip, P. J.; Clark, S. J.; Payne, M. C. *J. Phys.: Condens. Matter* **2002**, *14*, 2717; (b) Pickard, C. J.; Mauri, F. *Phys. Rev. B* **2001**, *63*, 245101.
13. (a) van Rossum, J.; Forster, H.; deGroot, H. J. M. *J. Magn. Reson.* **1997**, *124*, 516; (b) Lesage, A.; Emsley, L. *J. Magn. Reson.* **2001**, *148*, 449.
14. (a) Ashbrook, S. E.; Cutajar, M.; Pickard, C. J.; Walton, R. I.; Wimperis, S. *Phys. Chem. Chem. Phys.* **2008**, *10*, 5754; (b) Ashbrook, S. E.; Berry, A. J.; Frost, D. J.; Gregorovic, A.; Pickard, C. J.; Readman, J. E.; Wimperis, S. *J. Am. Chem. Soc.* **2007**, *129*, 13213; (c) Pallister, P. J.; Moudrakovski, I. L.; Ripmeester, J. A. *Phys. Chem. Chem. Phys.* **2009**, *11*, 11487.
15. Maringgele, W.; Meller, A.; Noltemeyer, M.; Sheldrick, G. M. *Z. Anorg. Allg. Chem.* **1986**, *536*, 24.
16. Greig, L.M. Ph.D. Thesis, University of St Andrews, 2001.
17. Stewart, J. J. P. *J. Mol. Model.* **2007**, *13*, 1173.
18. Fung, B. M.; Khitrin, A. K.; Ermolaev, K. *J. Magn. Reson.* **2000**, *142*, 97.
19. Brown, S. P.; Wimperis, S. *J. Magn. Reson.* **1997**, *124*, 279.
20. Pike, K. J.; Malde, R. P.; Ashbrook, S. E.; McManus, J.; Wimperis, S. *Solid State Nucl. Magn. Reson.* **2000**, *16*, 203.
21. Yates, J. R.; Pickard, C. J.; Mauri, F. *Phys. Rev. B* **2007**, *76*, 024401.
22. MOPAC2009 Stewart, J. J. P. *Stewart Computational Chemistry*; Colorado Springs: CO, USA, 2008;; http://OpenMOPAC.net.